Ultrasound in Med. & Biol., Vol. 43, No. 9, pp. 2000–2012, 2017

Printed in the USA
0301-5629/$ - see front matter

http://dx.doi.org/10.1016/j.ultrasmedbio.2017.03.021

● *Original Contribution*

IN VIVO MULTIPARAMETRIC ULTRASOUND IMAGING OF STRUCTURAL AND FUNCTIONAL TUMOR MODIFICATIONS DURING THERAPY

Alexandre Dizeux,* Thomas Payen,* Delphine Le Guillou-Buffello,* Eva Comperat,† Jean-Luc Gennisson,‡ Mickael Tanter,‡ Michael Oelze,§ and S. Lori Bridal*

* Sorbonne Universités, UPMC Univ Paris 06, CNRS, INSERM, Laboratoire d'Imagerie Biomédicale, Paris, France; † Academic Department of Pathology, Pitie-Salpetriere Hospital, AP-HP, UPMC Univ Paris 06, Paris, France; ‡ Institut Langevin—Ondes et Images, ESPCI ParisTech, PSL Research University, CNRS UMR7587, INSERM U979, Paris, France; and § Bioacoustics Research Laboratory, Department of Electrical and Computer Engineering, University of Illinois, Urbana, Illinois, USA

(*Received* 4 *October* 2016; *revised* 22 *March* 2017; *in final form* 27 *March* 2017)

Abstract—Longitudinal imaging techniques are needed that can meaningfully probe the tumor microenvironment and its spatial heterogeneity. Contrast-enhanced ultrasound, shear wave elastography and quantitative ultrasound are ultrasound-based techniques that provide information on the vascular function and micro-/macroscopic tissue structure. Modifications of the tumor microenvironment induced by cytotoxic and anti-angiogenic molecules in ectopic murine Lewis lung carcinoma tumors were monitored. The most heterogenous structures were found in tumors treated with anti-angiogenic drug that simultaneously accumulated the highest levels of necrosis and fibrosis. The anti-angiogenic group presented the highest number of correlations between parameters related to vascular function and those related to the micro-/macrostructure of the tumor microenvironment. Results suggest how patterns of multiparametric ultrasound modifications can be related to provide a more insightful marker of changes occurring within tumors during therapy. (E-mail: alexandre.dizeux@gmail.com) **© 2017 Published by Elsevier Inc. on behalf of World Federation for Ultrasound in Medicine & Biology.**

Key Words: **Multiparametric imaging, Ultrasound, Tumor, Elastography, Angiogenesis.**

INTRODUCTION

Throughout the course of tumor progression, the tumor microenvironment (TME) can evolve in a complex and heterogeneous manner to escape immunologic response and resist therapy. Multiple factors can contribute to creating a therapy-hostile TME such as insufficient microvascular and lymphatic networks, activated fibroblasts, suppressed immune response, hypoxia and acidity. To combat this, multipronged approaches have been proposed to render the TME more susceptible to therapy. For example, anti-angiogenic drugs can be used to transiently normalize the tumor microvascularization (remodel vessels such that tumor hypoxia and interstitial fluid pressure may be decreased) by better balancing the expression of pro- and anti-angiogenic factors. Reduced hypoxia and increased delivery of therapeutic agents associated with this approach can increase therapeutic efficacy. The possibility of permeabilizing collagen-rich tumors with anti-fibrosis drugs has also been investigated and has been found to improve delivery and efficacy of nano-medicines (Jain 2013).

Dynamically studying the modifications in the TME during tumor progression and therapy in pre-clinical models can guide the development and application of strategies aimed at modifying the TME to enhance therapeutic response. To accomplish this, longitudinal imaging techniques are needed that can meaningfully probe the TME and its spatial heterogeneity. Among the imaging techniques that are emerging to take on this challenge, ultrasound is of particular interest as a tolerable, portable (bedside) and repeatable imaging modality that can probe two key aspects of the TME: the microvascular network and the tumor stroma.

The functionality of tumor microvascularization can be assessed with contrast-enhanced ultrasound (CEUS) by injecting and detecting intravascular microbubbles (MBs) made of a gas encapsulated by a layer of lipids or phospholipids (Dietrich et al. 2012; Guibal et al. 2010; Hyvelin et al. 2013; Leen et al. 2012). Poor and heterogeneous microvascular perfusion within solid tumors can limit delivery of intravascularly delivered

Address correspondence to: Alexandre Dizeux, 17 rue moreau, Paris 75012. E-mail: alexandre.dizeux@gmail.com

drugs, restrict the immune response and produce hypoxic zones (Jain 2013). Another consequence of defective vascular and lymphatic networks coupled with the high metabolism of tumor cells is an increase in TME acidity caused by accumulation of carbonic acid that dissociates into bicarbonate and free protons (H^+). In a study in human patients, Williams et al. (2011) reported that functional CEUS could be used to evaluate anti-angiogenic therapy in renal cell carcinoma. Findings revealed a significant decrease in the fractional blood volume in treated patients (−73%).

Functional CEUS provides tracer-based detection of flow-filled regions, but traditionally cannot resolve individual vessels. The feasibility of mapping microvascular architecture with exceptional spatial resolution has recently been investigated in murine models with two very innovative CEUS-related techniques: contrast-enhanced acoustic angiography (Rao et al. 2016) and super-resolution vascular imaging (Errico et al. 2015). These techniques apply novel approaches to localize individual MBs within the vascular system, and by accumulation of many individual MB detections, a map of the microvascular tree is reconstructed. Thus, CEUS techniques are well positioned to provide more sensitive evaluation of tumor extent and a non-invasive assessment of the microvascular flow within regions of tumors. Vascular tortuosity, which can be assessed with CE-acoustic angiography, and super-resolution techniques may ultimately provide new indices related to tumor progression and interstitial fluid pressure (Hompland et al. 2012).

The tumor stroma consisting of loose connective tissue, blood vessels and nerves has both structural and biological impacts on tumor progression. The extracellular matrix (ECM) can generate forces within the tumor to compress blood and lymphatic vessels (Jain 2013). The ECM and pericyte coverage influence the passage of intravascularly delivered drugs (Nakasone et al. 2012). Activated fibroblasts are associated with increased proliferative activity and enhanced secretion of ECM proteins such as type I collagen and fibronectin. Structural modifications of the TME can affect the elastic properties of tumor tissues, which can be monitored *in vivo* by generating shear waves and monitoring their propagation with ultrafast imaging (Tanter and Fink 2014). In patient studies, shear wave elastography (SWE) helped to predict chemotherapy efficiency in breast lesion treatment (Athanasiou et al. 2015) and to differentiate between the stiffness of normal brain tissue, low-grade glioma and high-grade glioma (Chauvet et al. 2015). Chamming's et al. (2013) evaluated the relationship between SWE measurements and histologic indices in a model for human invasive ductal carcinoma (HBCx-3). They reported a significant negative correlation between tumor stiffness and the percentage of necrosis ($r = -0.76$, $p = 0.0004$) and a very significant positive correlation between tumor stiffness and the percentage of fibrosis ($r = 0.83$, $p < 0.0001$). These results suggest that necrotic and fibrotic tissues are related, respectively, to soft and stiff media. Chamming's et al. also reported a strong correlation between the size of the tumor and its stiffness ($r = 0.94$, $p < 0.0001$), which was explained, for their model, by higher fibrosis in the larger tumors.

Furthermore, the underlying microstructure of tumor stroma can be evaluated using quantitative ultrasound (QUS) through calibrated spectral analysis of raw, radiofrequency ultrasonic echoes scattered from the tissue (Vlad et al. 2009). Several studies have found that QUS techniques are sensitive to changes in tissue microstructure consistent with cell death associated with response of tumors to therapy (Kemmerer et al. 2013; Kolios and Czarnota 2009; Kolios et al. 2002; Vlad et al. 2008, 2009, 2010, 2011). Cell death, and more specifically apoptosis or programmed cell death, is associated with the response of tumors to therapy. Most cytotoxic anticancer agents induce apoptosis, and evidence suggests that defects in apoptotic programs in cells contribute to the failure of a tumor to respond to treatment (Lowe and Lin 2000). Therefore, by having sensitivity to the presence or absence of apoptosis and cell death in a tumor, QUS techniques provide an ideal imaging technique for detecting and quantifying tumor responses to therapy. More recently, QUS techniques were reported to detect early response to breast cancer therapy in a limited trial in 30 human patients (Sannachi et al. 2015). In that study, parametric models of the backscattered power spectra were used to predict the response of patients to chemotherapy as soon as 1 wk post-therapy. Specifically, the effective scatterer diameter (ESD) and effective acoustic concentration (EAC) were estimated for patients undergoing treatment. The best prediction of treatment response was achieved with the combination of EAC and ESD at week 4 (82% sensitivity, 100% specificity and 86% accuracy) over a 12- to 18-wk course of treatment.

Ideally, biomarkers need to provide a broad range of information on the tumor microenvironment and its heterogeneity so that the most appropriate therapies are selected and the therapeutic response is assessed based on a tumor's functional, molecular and heterogeneity profile. A potential wealth of information related to the tumor microenvironment is offered by *in vivo* ultrasonic imaging modes, but there is a lack of understanding concerning the specific changes in the tumor that modify each imaging parameter and correlations between the different imaging parameters. Such understanding is necessary to develop an integrated exploitation of the image-based information in the diagnostic and therapeutic decision-making processes. Quantitative measurements made with a range of imaging techniques under matched conditions in an animal model allowing

comparison of imaging data with invasive reference techniques are thus needed to move toward multimodal imaging biomarkers characterizing the TME.

The goal of this study was to evaluate the sensitivity and complementarity of CEUS, SWE and QUS in characterizing modifications of the TME during therapy with a cytotoxic agent (cyclophosphamide), an angiogenesis inhibitor (sunitinib, Sutent: SU11248) and placebo in ectopic, murine Lewis lung carcinoma (LLC) tumors. Imaged data were compared with evaluation of fibrosis and necrosis by an expert pathologist. *In vivo* and *ex vivo* follow-up of TME modifications should provide a better understanding of how ultrasound imaging modes reflect changes in the tumor produced by a cytotoxic drug (cyclophosphamide) versus changes resulting from anti-angiogenic treatment (sunitinib).

METHODS

Tumor cell implantation and treatment

Animal studies were approved by the Charles Darwin ethical committee (ref: Ce5/2012/081). LLC fragments (20–40 mm^3) were implanted in the right flank of 7-wk-old female C57 Bl/6 J mice (Janvier Labs, St. Berthevin, France). Surgery was performed under anesthesia with 2% isoflurane and subcutaneous injection (pre- and post-operative) of buprenorphine analgesic at a concentration of 0.05 mg/kg. The temperature of the animal was maintained during anesthesia using a thermostatic, heated support (Minerve, Esternay, France).

Six days after fragment implantation, the animals were randomly assigned to three treatment groups receiving: sunitinib (SU11248, Sutent, Pfizer, USA), an angiogenesis inhibitor that targets vascular endothelial growth factor (VEGF) and platelet-derived growth factor (PDGF) receptor signaling (40 mg/kg/d orally for 13 d, n = 21) (Mendel et al. 2003); cyclophosphamide (C7397-1 G, Sigma-Aldrich, France), an alkylating cytotoxic agent (150 mg/kg injected intraperitoneally for 3 d, n = 24) (Wang et al. 2007); and placebo (100 μL of phosphate-buffered saline [PBS] injected intraperitoneally for 3 d, n = 24). Imaging as described in the subsequent sections was performed to follow tumor development for 13 d, beginning just before the initiation of therapy. The 13-d endpoint was chosen based on known tumor growth rates to ensure that tumor volume remained below limits related to the respect of animal well-being.

Shear wave elastography

Stiffness measurements were carried out with a clinical ultrasound system (Aixplorer, SuperSonic Imagine, Aix en Provence, France) using an SL15-4 probe with 256 elements, 0.2-mm pitch, a bandwidth of 4–15 MHz and a central frequency of 8 MHz. For each tumor, SWE data were acquired from three independent planes along both the longitudinal and transverse directions (six SWE measurements per tumor). Data were acquired using penetration mode with a color scale ranging from 0 to 50 kPa; the mean value and standard deviation (SD) of stiffness were assessed within a region of interest (ROI) from each imaging plane, and then the average of each parameter from the six independent planes was calculated (Fig. 1a). This operation performed over the SD yields the factor of heterogeneity within the tumor.

Before the SWE acquisition, the tumor dimensions were assessed on B-mode images. Tumor volume was approximated using the ellipsoid formula $V = (\pi/6)abc$, where a is the length, b is the width and c is the thickness.

Quantitative ultrasound

Radiofrequency signals were acquired in two perpendicular planes (planes 1 and 4, Fig. 1d) with the same clinical ultrasound system and SL15-4 probe. Probe settings were set on "research mode" with the emitted frequency at 11.25 MHz.

Before performing RF data processing, it was necessary to acquire RF signals from a reference phantom whose physical properties (backscatter coefficient and attenuation) were well characterized. A reference phantom was purchased (University of Wisconsin, Madison). The attenuation coefficient in the phantom was quantified by the manufacturer. The backscatter coefficient from the reference phantom was estimated using a planar reference technique (Chen et al. 1997). The calibrated characteristics of the phantom are summarized in Figure 2.

Quantitative ultrasound parameters were mapped throughout each tumor by analyzing 3 × 3-mm blocks of data with a 75% overlap in the axial and lateral directions (Fig. 1c). The average backscattered power spectrum was calculated for each data block based on the Fourier transform (512 points) of the Hanning gated segments of RF data from each data block. These data were normalized with respect to the data from the corresponding region of the reference phantom, and correction for attenuation in the propagation path was applied assuming that the attenuation and sound speed in the tumor were 0.4 dB/cm/MHz and 1540 m/s, respectively. Two QUS parameters were estimated based on the backscatter coefficient versus frequency: the ESD (μm) and the EAC (dB/cm) using a spherical Gaussian model.

Contrast-enhanced ultrasound

Contrast imaging was performed with a second clinical ultrasound system (Sequoia 512, Acuson, Siemens, Mountain View, CA, USA) with a broadband 7- to 14-MHz transducer in cadence contrast pulse sequencing mode. Dynamic CEUS clips in DICOM JPEG formatted

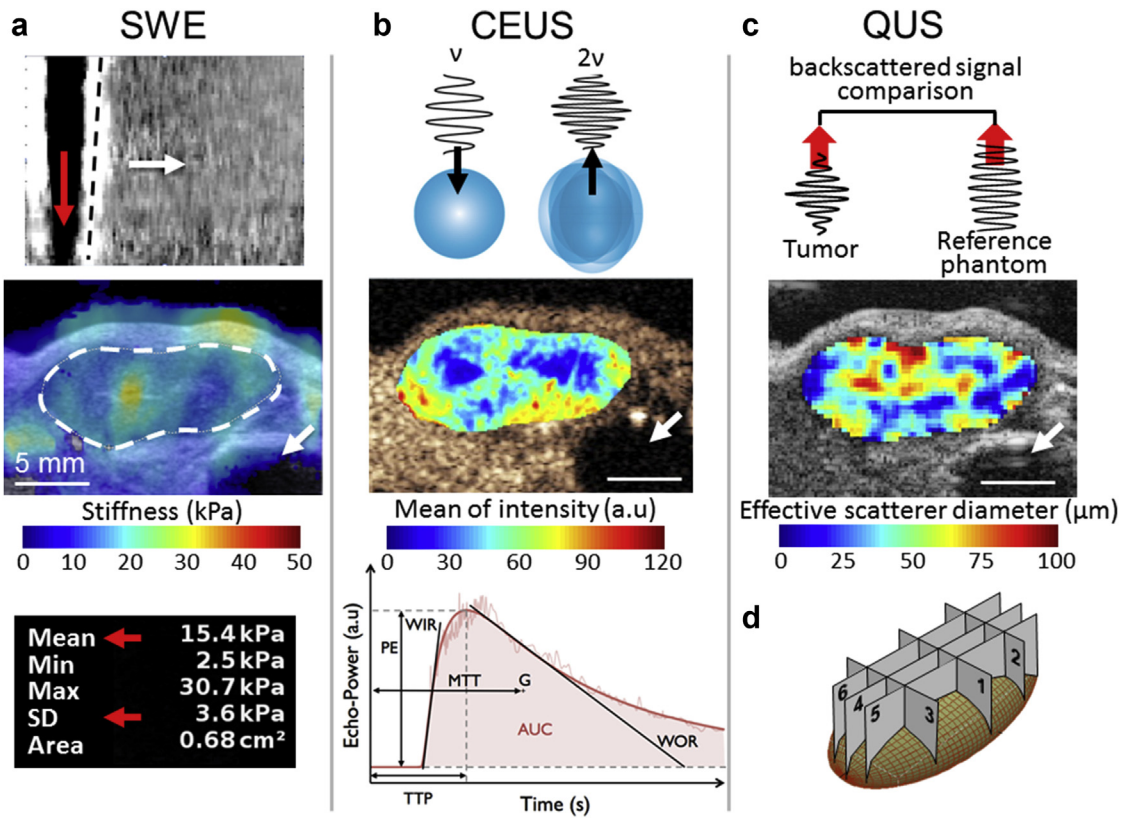

Fig. 1. Summary of the ultrasound imaging modalities. (a) By focusing ultrasound at different depths (pushing beam, *red arrow*) a shear wave (*dashed line*) is generated that propagates perpendicularly (*white arrow*) with respect to the propagation direction of the imaging beam. The propagation speed of this wave, as assessed using ultrafast imaging, is directly related to the stiffness of the medium in which it propagates. The mean and standard deviation (SD) of the shear wave elasticity (SWE) were quantified within regions of interest selected on B-mode images to delineate the full cross section of the tumor. (b) The echo power from the non-linear response of the ultrasound contrast agent SonoVue was analyzed as a function of time to map the functionality of the tumor microvasculature. (c) The size of effective scatters in the tumor was estimated using quantitative ultrasound (QUS) by comparing the backscattered signal from the tumor with that from a reference phantom using estimation voxels of 1 × 1 mm. (d) Average SWE was evaluated from the six planes, QUS was assessed and averaged from planes 1 and 4 and the contrast-enhanced ultrasound (CEUS) sequence was calculated from perfused zones of plane 4. *White arrows* indicate the position of the bladder in each image. AUC = area under the curve; MTT = mean transit time; PE = peak enhancement; TTP = time or peak; WIR = wash-in rate; WOR = wash-out rate.

files were acquired with a dynamic range of 80 dB at a frame rate fixed at 1 Hz and a mechanical index equal to 0.1 to minimize destruction of microbubbles. Caudal vein injections (0.5 mL/kg in 40 μL) of the ultrasound contrast agent SonoVue (Bracco Suisse, Geneva, Switzerland) were made using a controlled injection system (Dizeux et al. 2016). The image plane was positioned along the maximum longitudinal plane of the tumor

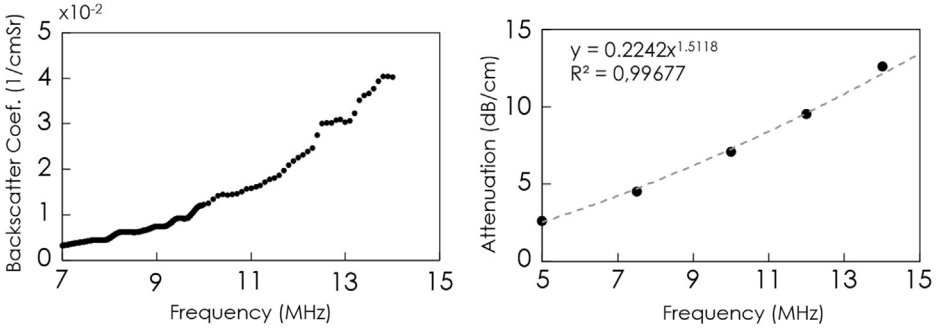

Fig. 2. Backscatter coefficient and attenuation of the phantom used as a reference medium in this study to normalize backscattered signals acquired from tumors.

(plane 4, Fig. 1d). A B-mode image of the central plane that had been previously selected for SWE and QUS measurements was displayed for visual comparison to help the operator re-align the plane position for CEUS as closely as possible with the previously studied region. Data were acquired from the instant before bolus injection up to 180 s after the injection. Average echo power was initially measured in a region of interest including the total tumor cross section. Regions with no contrast enhancement were identified to assess the percentage of the tumor cross section that was unperfused. All unperfused regions were then excluded from further analysis, and the echo power from the perfused region was measured (Payen et al. 2013). A lognormal bolus model was fit to the resulting echo-power curve to assess flow within the perfused region of the tumor (Hudson et al. 2015; Payen et al. 2015). Fits were made using a maximum likelihood estimator which is well adapted to the multiplicative nature of the noise that corrupts CEUS and B-mode images (Barrois et al. 2013). Several flow parameters were estimated (Fig. 1b): peak enhancement (PE), mean transit time (MTT), time to peak (TTP), wash-in (WIR) and wash-out (WOR) rates and area under the curve (AUC).

Immunohistochemistry

Two tumors per group were prepared for hematoxylin erythrosine saffron (HES) and Sirius red staining to reveal necrosis and fibrosis, respectively, at day 9 after the beginning of therapy. Remaining tumors that were not used for other analyses were prepared for histology at the end of therapeutic follow-up, on day 13: angiogenesis inhibitor (n = 14), cytotoxic agent (n = 8) and placebo (n = 19). Blind evaluation of histologic slides was made by a pathologist with 12 y of experience.

Statistics

All statistical tests and analysis were performed using R software (Version 3.1.1). To determine whether the means from the three different groups differed statistically, an analysis of variance (ANOVA) was performed. If the ANOVA *F*-test revealed a significant difference between groups, then a pairwise *t*-test with a Bonferroni adjustment was performed between each pair of groups. A Wilcoxon signed-rank non-parametric test (Mann–Whitney *U*-test) was used to compare the results within each group between baseline and the last day of follow-up (paired test). Differences were considered significant at $***p < 0.005$, $0.005 < **p < 0.01$ and $0.01 < *p < 0.05$. CEUS, SWE and QUS parameters are expressed as the mean ± SD. The Pearson correlation test was carried out to assess the correlation between all parameters measured *in vivo* and *ex vivo*. The data were visualized as boxplots depicting the minimum, lower quartile, median, mean value (square), upper quartile and maximum values.

RESULTS

Tumor volumes are summarized in Figure 3. From day 3 after the beginning of therapy, tumor volume (20 ± 10 mm^3) was significantly lower for the group treated with the cytotoxic agent than for the group that received the angiogenesis inhibitor (42 ± 24 mm^3, $p = 0.007$) and the placebo group (37 ± 16 mm^3, $p = 0.04$). This difference was maintained throughout the follow-up to day 13 (192 ± 253 mm^3) versus the anti-angiogenic group (635 ± 330 mm^3, $p = 0.0004$) and the placebo group (882 ± 280 mm^3, $p < 0.0001$). Tumor volume for the group receiving placebo was not significantly higher than for the group treated with the angiogenesis inhibitor.

Shear wave elastography measurements are illustrated in Figure 4. From day 7 after the beginning of therapy, tumor stiffness for the group receiving the angiogenesis inhibitor (14.1 ± 3.6 kPa) was significantly higher than that for the group receiving the cytotoxic agent (9.8 ± 2.8 kPa, $p < 0.0001$) and the placebo group (12.0 ± 2.4 kPa, $p = 0.04$). Differences remained significant from days 7 to 13 (anti-angiogenic vs. cytotoxic, $p = 0.006$; vs. placebo, $p = 0.04$). From days 7 to 13, tumors treated with the angiogenesis inhibitor exhibited a higher level of stiffness heterogeneity (day 13: 10.8 ± 2.4 kPa) compared with those receiving cytotoxic agent (3.6 ± 2.5 kPa, $p = 0.0004$) and placebo (3.6 ± 2.5 kPa, $p = 0.02$).

From baseline to day 3, most of the tumors were too small (<4 mm) for assessment of the backscatter coefficient with QUS methods. Thus, QUS measurements were only performed only from days 7 to 13 (Fig. 5). At

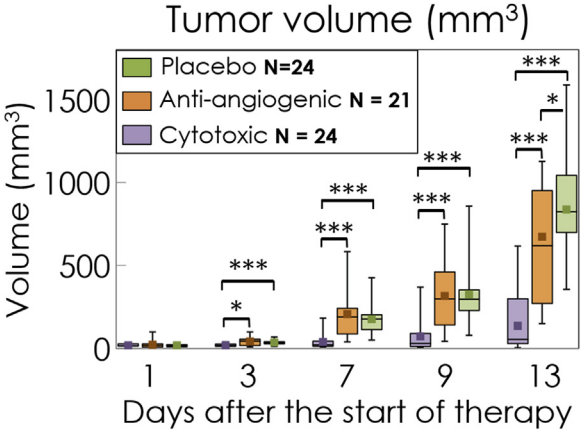

Fig. 3. Longitudinal follow-up of tumor volume estimated for an ellipsoid with axis lengths equal to measurements made along the longitudinal, transversal and thickness of the tumor. Cytotoxic agent: N = 24; anti-angiogenic agent: N = 21; placebo: N = 24. * = $0.01 < p < 0.05$. *** = $p < 0.005$.

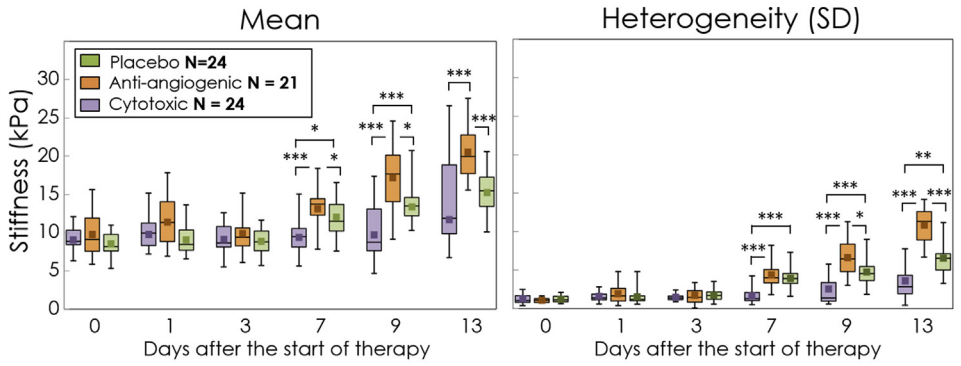

Fig. 4. Tumor stiffness assessed with shear wave elastography. Six measurements were performed in six different planes for each tumor and averaged. Heterogeneity of the stiffness for each tumor was estimated based on the average standard deviation of the stiffness within the six regions of interest. Cytotoxic agent: N = 24; anti-angiogenic agent: N = 21; placebo: N = 24. * = $0.01 < p < 0.05$. ** = $0.005 < p < 0.01$. *** = $p < 0.005$.

day 7, no significant difference in ESD and EAC parameters was observed between groups. At day 13, the anti-angiogenic group had a higher mean ESD (77 ± 13 μm) compared with the cytotoxic (65 ± 19 μm, $p = 0.1$) and placebo (51 ± 12 μm, $p < 0.005$) groups. At day 13, the anti-angiogenic group had a lower EAC (5 ± 6 dB/cm) compared than the placebo (27 ± 18 dB/cm, $p < 0.001$) and cytotoxic (17 ± 11 dB/cm, $p = 0.16$) groups.

Figure 6 summarizes the results from CEUS analysis of the tumor's microvascular function. The temporal changes in the percentage of unperfused area ($ROI_{unperfused}/ROI_{tumor}$) in tumor was significantly higher for the group treated with the angiogenesis inhibitor (3.1 ± 3.9%) from day 7 than for the groups that received the cytotoxic agent (0%, $p = 0.002$) and placebo (0%, $p = 0.0008$). The unperfused area in tumors treated with the angiogenesis inhibitor strongly increased at day 13 (29 ± 21%), and this value remained significantly higher compared with the values for the cytotoxic (7.3 ± 15%, $p = 0.004$) and placebo (7.5 ± 13%, $p = 0.003$) groups.

Within the perfused area of the tumors, several functional parameters significantly differed between groups. Peak enhancement, related to blood volume, was significantly lower at day 13 for the angiogenesis-inhibited group (0.21 ± 0.12 au) than for the cytotoxic agent group (0.41 ± 0.22 au, $p = 0.002$). The angiogenesis-inhibited group approached a significant difference relative to the placebo group (0.28 ± 0.14 au, $p = 0.06$).

From days 7 to 9, the MTT of the anti-angiogenic group (MTT_{Day7} = 32.3 ± 3.4 s, MTT_{Day9} = 35.3 ± 5.8 s) was significantly higher than those for the cytotoxic (MTT_{Day7} = 29.1 ± 2.2 s, $p = 0.02$; MTT_{Day9} = 29.2 ± 3.1 s, $p = 0.0009$) and placebo (MTT_{Day7} = 29.5 ± 3.3 s, $p = 0.03$; MTT_{Day9} = 31.6 ± 3.8 s, $p = 0.05$) groups. Afterward, the MTT value remained at a similar level in the cytotoxic group (MTT_{Day13} = 29.7 ± 3.9 s) and was significantly lower compared

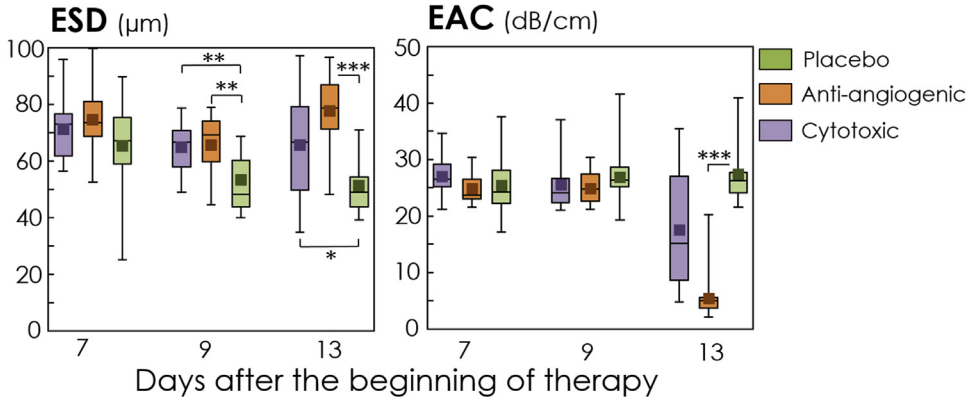

Fig. 5. Effective scatterer density (ESD) and effective acoustic concentration (EAC) parameters measured by quantitative ultrasound from days 7 to 13. The anti-angiogenic group has a higher mean ESD value compared with the other groups but the threshold of significance was only reached for the comparison with the placebo group. The mean value of EAC parameter was significantly lower for the anti-angiogenic group compared than for the control. * = $0.01 < p < 0.05$. ** = $0.005 < p < 0.01$. *** = $p < 0.005$.

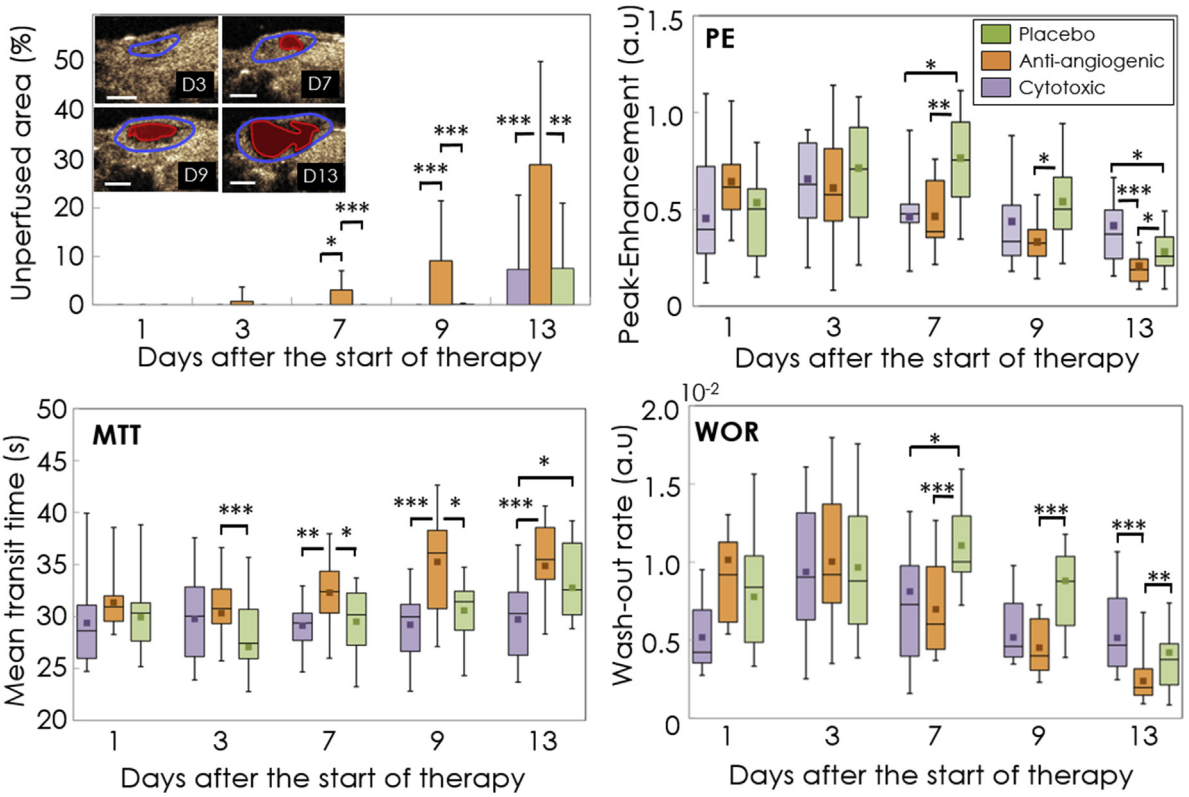

Fig. 6. Results of the follow-up performed in contrast-enhanced ultrasound imaging. Evolution of the unperfused area, peak enhancement (PE), mean transit time (MTT) and wash-out rate (WOR) are provided for the cytotoxic (N = 15), anti-angiogenic (N = 16) and placebo groups (N = 18). * = $0.01 < p < 0.05$. ** = $0.005 < p < 0.01$. *** = $p < 0.005$.

with the values for both the anti-angiogenic group (MTT_{Day13} = 36.2 ± 4.9 s, p = 0.001) and the placebo group (MTT_{Day13} = 34.7 ± 5.3 s, p = 0.01).

Finally, the wash-out rate in tumors treated with the angiogenesis inhibitor decreased significantly at day 13 (0.0024 ± 0.0015 au) compared with the value for the tumors treated with cytotoxic agent (0.0052 ± 0.0023 au, p = 0.007), but the difference was not significant compared with the value for the placebo group (0.0042 ± 0.0025 au, p = 0.2).

The percentages of necrosis and fibrosis as assessed by a blinded pathologist on histologic sections are illustrated in Figure 7. At day 13, the levels of necrosis and fibrosis, respectively, in the group treated with the angiogenesis inhibitor (n = 14, HES = 20.5 ± 11.3%; Sirius red = 14.5 ± 9.9%) were significantly higher than those for the cytotoxic (n = 8, HES = 7.8 ± 5.3%, p = 0.002; Sirius red = 5.6 ± 5.0%, p = 0.04) and placebo (n = 19, HES = 7.6 ± 5.5%, p = 0.0001; Sirius red = 6.4 ± 6.9%, p = 0.01) groups. There was no significant difference between the levels of necrosis and fibrosis at day 13 between the cytotoxic and placebo groups.

The correlation between parameters was evaluated for each therapeutic group (Fig. 8). Parameters were divided into two different classes: one class is related to vascular function, and the other class is related to microscopic and macroscopic structure. The upper left quadrant of each panel confirms that there were significant correlations between several of the functional CEUS indices that remained consistent from one therapy group to another. Similarly, the lower right quadrant contains correlations among many of the structural parameters. The two quadrants outlined in pink in each panel revealed that the number of correlations occurring between functional and structural parameters was very low in the relatively homogeneous tumors treated with cytotoxic therapy and was highest in the most heterogeneous tumors treated with anti-angiogenic therapy. More specifically, within both the placebo and the anti-angiogenic groups, the SD SWE increased as blood flow markers assessed for the full tumor decreased (PE, WOR, AUC), the tumor size increased and the perfused area decreased. Within the anti-angiogenic group, as CEUS markers of blood flow decreased, the mean EAC decreased and the mean SWE increased. In the anti-angiogenic group, where inter-correlations of the functional and structural imaging parameters were high, increased fibrosis as evaluated on histologic specimens (14.5 ± 9.9%) was associated with a strong reduction

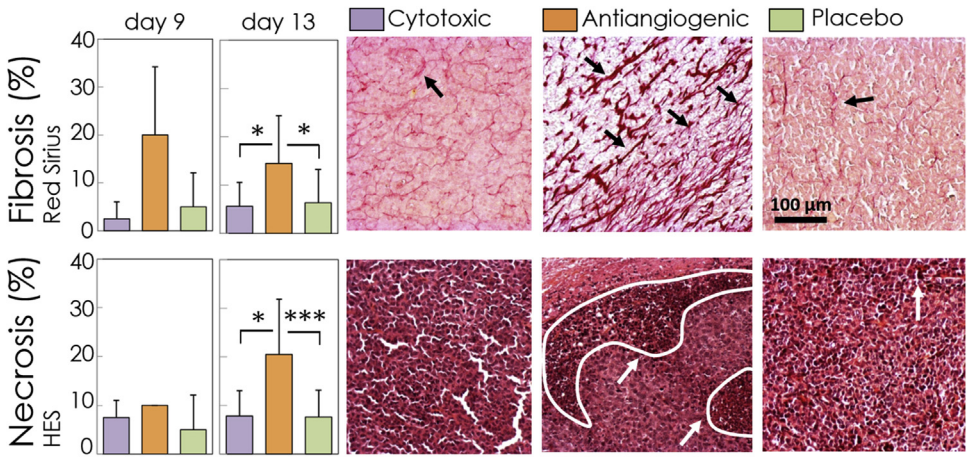

Fig. 7. Fibrosis and necrosis as assessed from histology at day 9 (n = 2 for all groups) and day 13 (cytotoxic: n = 8, antiangiogenic: n = 14, placebo: n = 19). Stained sections from day 13 using, respectively, Sirius red and hematoxylin erythrosine saffron (HES) staining. *White and black arrows* designate necrotic and fibrotic areas, respectively. ×20. * = $0.01 < p < 0.05$. *** = $p < 0.005$.

in EAC from day 9 to day 13 (anti-angiogenic: −79%, cytotoxic: −31% and placebo: +2%). More complex patterns of imaging parameter changes need to be considered for the placebo and anti-angiogenic groups. As tumor size progressed in both of these groups, the SD SWE increased, and the perfused area as assessed with CEUS decreased. This pattern of related image-parameter modifications could provide a useful marker of devascularization and formation of necrotic zones within the tumor. Some difference in the process of the vascular changes may be hinted at by the additional inter-parameter correlations observed within the anti-angiogenic group. Reduced EAC and increased mean SWE were observed with increasing tumor size in the anti-angiogenic group.

DISCUSSION

Longitudinal follow-up of tumor modifications was performed *in vivo* using CEUS, SWE and QUS and *ex vivo* with immunohistochemistry to better understand how ultrasound imaging modes reflect tumoral modifications resulting from either a cytotoxic drug (cyclophosphamide) or an anti-angiogenic treatment (sunitinib).

Histology

Histologic results were consistent with the results of Bozkurt et al. (2011), who reported a high level of fibrosis using sunitinib in an encapsulating peritoneal sclerosis model in rat. In another study, Broutin et al. (2011) used sunitinib in a xenograft tumor model of a medullary thyroid carcinoma and reported increases in the level of necrosis and fibrosis by factors of 1.3 and 2.2, respectively, compared with untreated mice. The development of necrotic tissues in tumor is due principally to ischemic processes that prevent oxygen from reaching tumor cells. The main macromolecules making up the 3-D meshwork of the ECM are the fibrous proteins (collagen and elastin:

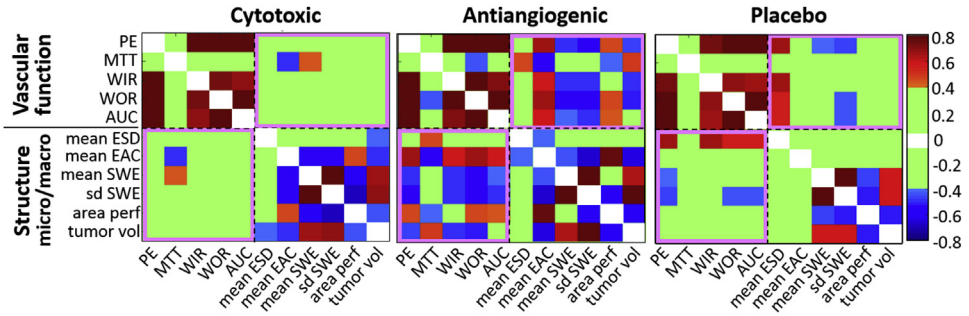

Fig. 8. Correlation tables for all parameters in full-tumor regions of interest for each of the three groups: cytotoxic, anti-angiogenic and placebo. The self-correlations along the diagonal axes are in *white*. All correlations with non-significant p values and all correlations between −0.4 and 0.4 are mapped in *pale green* background color to enhance visual contrast of the correlations of interest. Significant ($r > 0.4$) positive Pearson correlations are mapped in *reds*, and negative correlations, in *blues*. The *pink*-outlined quadrants correspond to correlations between indexes related to the microvascularization (vascular function) and those related to the tumor stroma (microscopic and macroscopic structure).

structural role, fibronectin and laminin: adherence role) and polysaccharides (glycosaminoglycan and proteoglycans: retention of cytokine and growth factors). The ECM controls the physiologic equilibrium of the medium by synthesizing and degrading its components. The development of fibrosis is linked to a rupture of this equilibrium by which the ECM increases synthesis of its constituents and at the same time decreases their degradation. The fact that sunitinib significantly increased the level of fibrosis and necrosis without strongly modifying tumor volume is consistent with the anti-angiogenic effect, not only on tumor cells, but also on their microenvironment. This effect is thought to be due to the potent inhibition of angiogenesis by tyrosine kinase-inhibiting receptors such as VEGFR2, PDGFRa and PDGFRb. These results are corroborated by Huang et al. (2010), who reported that sunitinib inhibited renal cell carcinoma (RCC) xenograft growth mainly though anti-angiogenic mechanisms and not through direct targeting of RCC tumor cells, as no significant reduction of the tumor volume was observed.

Functional dynamic contrast-enhanced magnetic resonance imaging (DCE-MRI) and *ex vivo* analysis of necrotic level, hemorrhage and vascular anatomy were previously used to evaluate changes in renal cell carcinoma xenografts during therapy with sunitinib at 20 and 40 mg/kg/d (Hillman et al. 2009). At 20 mg/kg/d, renormalization of tumor microvessels was observed and perfusion was enhanced in the group receiving sunitinib compared with the group receiving placebo. Histologic assessment of the treated tumors revealed more regular and thinner vessels in the group receiving anti-angiogenic therapy. At 40 mg/kg/d (consistent with the dose administered in our model), perfusion of the microvessels in the group receiving sunitinib was significantly reduced compared with that in both the placebo and lower dose sunitinib groups. Histology revealed large areas of necrosis associated with hemorrhage. Although direct comparisons cannot be made because two different tumor models were considered, these results are consistent with the types of modifications seen in our model.

Microstructure assessment: Shear wave elastography and quantitative ultrasound

The high mean stiffness of tumors in the anti-angiogenic group compared with the other groups in our study (Fig. 4, days 9 and 13), was associated with higher fibrosis (Fig. 7). These results can be compared with those of Chamming's et al. (2013), who used human invasive ductal carcinoma (HBCx-3) without any therapy to determine the relationship between SWE measurement in tumor and histologic outcomes. They reported that there was a significant negative correlation between tumor stiffness and the percentage of necrosis ($r = -0.76$, $p = 0.0004$) and a very significant positive correlation between tumor stiffness and the percentage of fibrosis ($r = 0.83$, $p < 0.0001$). These results suggest that necrotic and fibrotic tissues are related, respectively, to soft and stiff medium. We observed the trend linking stiff tumor and fibrosis in our study with stiffest tumor for the group with the highest amount of fibrosis (anti-angiogenic). The anti-angiogenic group also exhibited the most heterogeneous mixture of necrosis and fibrosis. This heterogeneity was reflected *in vivo* by higher values in the SD SWE standard deviation across the tumor treated with sunitinib compared with the other treatments (Fig. 4b at day 13).

Chamming's et al. also reported a strong correlation between the size of the tumor and its stiffness ($r = 0.94$, $p < 0.0001$) which was explained, for their model, by higher fibrosis in the larger tumors. A similar relationship between size and stiffness was highlighted in our study in ectopic LLC tumors. Figure 9 illustrates SWE measurements in control tumors, revealing a significant correlation between SWE and tumor volume ($r = 0.80$ with $p < 0.005$).

Jugé et al. (2012) characterized the effect of an anti-vascular drug (combretastatin, CA4*p* at 100 mg/kg) on a colorectal carcinoma (CT26) using diffusion-weighted (apparent diffusion coefficient) and elastography MRI. They reported a significant drop in tumor stiffness 24 h after treatment (from 6.6 ± 0.8 to 4.8 ± 0.7 kPa, $p = 0.0001$). The authors explained this drop in tumor stiffness as the consequence of a significant reduction in mean vessel density evaluated using CD31 staining to compare the vessel density in the viable area of the treated group with that in the control group (299 ± 37 [1/mm^2] vs. 208 ± 66 [1/mm^2], $p = 0.03$). A significant increase in cellularity was also observed in the treated group. In consideration of the work of Chamming's et al. (2013), who reported an inverse correlation between tissue stiffness and the level of necrosis, it could be argued that the drop in tumor stiffness observed in the work of Jugé et al. could also be attributed

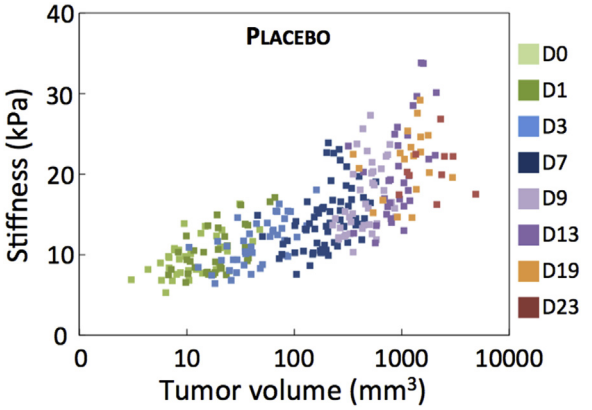

Fig. 9. Correlation between stiffness and tumor volume for placebo-treated tumors ($r = 0.80$, $p < 0.005$, measurements from 280 tumors).

to the significant increase in necrosis from 7 ± 2% to 43 ± 3% observed 24 h after CA4p administration.

For QUS parameters, the fact that the anti-angiogenic group had higher mean values for ESD seems consistent with the histology presented in Figure 7. Indeed, tumors were observed to form thicker fibrotic structures in the group treated with the anti-angiogenic agent than in the other treatment groups. The EAC correlated negatively with fibrosis in the tumors studied invasively by histology in the cytotoxic group. Within the group of tumors treated with anti-angiogenic therapy, EAC increase correlated with increasing tumor size. These results appear to suggest that the QUS parameters are most sensitive to the fibrotic tissue in this tumor model, but further analysis is necessary to confirm this hypothesis.

Another recent study (El Kaffas et al. 2015) evaluated QUS parameter changes in breast tumor xenografts (MD1-MB-231) during radiation therapy alone or after pre-treatment with either sunitinib (30 mg/kg/d) or a vascular protecting agent. El Kaffas et al. suggested that changes observed in the QUS parameter referred to as "midband fit" were related to decreases in the vascular density and the smaller number of hypoxic regions observed in associated histologic sections. Although no direct comparison can be between the results of El Kaffas et al. and our results because of the different therapies and tumor models used, the fact that different QUS parameters were selected to track changes within the tumor considered to be related to changes in different structures within the tumors (fibrosis and vascular properties, respectively) underlines that patterns that are identified in one tumor/therapy model may not be readily extended to others.

Microvascular assessment: Contrast-enhanced ultrasound

Contrast-enhanced ultrasound imaging allowed assessment of the state of the vascular and microvascular network by measuring flow parameters after a bolus injection of contrast agent. Parameters such as PE and AUC are related to blood volume, whereas MTT, TTP, WOR and WIR parameters are directly related to the functionality of the vascular network.

The contrast enhancement was characterized in two complementary ways. First, a measurement of the percentage of the non-perfused area provided information on overall vascularization. For the evaluation of quantitative flow assessments, however, time–intensity curves need to be obtained from regions of flow that are as homogeneous as possible. Otherwise, parameters calculated from the curves will not reflect the real kinetics of the microbubbles within the functional tumor vasculature. Thus, for functional parameter assessment, regions of the tumor with no contrast during the sequence were excluded from the measurement zone. We have used a similar approach in previous work (Payen et al. 2015), and others have also underlined the need to consider spatial heterogeneity of the perfusion in tumors when using dynamic CEUS (Hudson et al. 2015).

The blood volume (PE parameter) was significantly lower for tumors treated with sunitinib than for those treated with the cytotoxic agent and drug vehicle at day 13 (Fig. 6, PE). Several studies using different contrast imaging modalities reported the same trend of a decrease in blood volume in murine carcinoma treated with sunitinib (Battle et al. 2011; Matsumoto et al. 2011, 2014; Needles et al. 2013)

Our histologic results at day 13 revealed high levels of necrosis and fibrosis for tumors treated with the anti-angiogenic drug compared with those treated with the cytotoxic agent and drug vehicle (Fig. 7). At the same time, during therapeutic follow-up, the percentage of unperfused area was significantly higher in the anti-angiogenic group than in the cytotoxic and placebo groups (Fig. 6). The evolution of the unperfused area versus the percentage of necrosis was thus further evaluated based on correlations for 45 mice with *in vivo* and *ex vivo* measurements made on the same day. The unperfused area correlated much more strongly with the percentage of necrosis ($r = 0.71$, $p < 0.005$) than with the percentage of fibrosis ($r = 0.22$, $p = 0.15$).

The functionality of the microvascular network that remained perfused at day 13 was strongly affected by the anti-angiogenic therapy (Fig. 6). Values of MTT and WOR parameters were respectively the highest and the lowest for tumors treated with sunitinib, indicating that the contrast agent remained longer in the vasculature (high MTT) partly because vessels had difficulty to draining off (low WOR) the microbubbles. These results indicate that the microvascular networks of tumors treated with sunitinib became significantly less efficient than those of tumors treated with cytotoxic agent and drug vehicle (placebo). Faivre et al. (2007) proposed a mechanism to explain the modification of tumor vasculature and the development of necrosis induced by sunitinib. In an established tumor, angiogenesis supplies cancer cells with oxygen, growth factors and nutrients. Exposure of the tumor to sunitinib alters endothelial cell shape and induces detachment of the endothelial cells from the substratum. Endothelial cell loss leads to blood vessel congestion and reduced blood flow. As a result of the lack of oxygen, growth factors and nutrients, tumor necrosis ensues (Faivre et al. 2007). This mechanism of action is consistent with observations based on our histologic results of high levels of necrosis and fibrosis in the sunitinib group. It is also consistent with

Table 1. Variation in mean values of SWE and CEUS parameters between baseline and day 13 for each group*

	Cytotoxic agent		Anti-angiogenic agent		Placebo	
	Variation (%)	*p* value	Variation (%)	*p* value	Variation (%)	*p* value
Shear wave elastography						
Mean (kPa)	20†	0.036	80†	<0.0001	69†	<0.0001
SD (kPa)	130†	0.004	470†	<0.001	330†	<0.001
Contrast-enhanced ultrasound						
PE (au)	−8.7	0.892	−68†	<0.0001	−48†	0.002
WIR (au)	−39	0.162	−83†	<0.0001	−78†	<0.0001
WOR (au)	−0.2	0.545	−76†	<0.0001	−46†	<0.001
MTT (s)	1.1	0.650	15†	0.004	17*	0.003

CEUS = contrast-enhanced ultrasound; MTT = mean transit time; PE = peak enhancement; TTP = time to peak; SD = standard deviation; SWE = shear wave elastography; WIR = wash-in rate; WOR = wash-out rate.
* Variation = $(MV_{D13}/MV_{D1}-1) \times 100$, where MV_{D13} is the mean value of the parameter at day 13, and MV_{D1} the mean value of the parameter at day 1.
† Significant difference from days 1 to 13. *p* Values were calculated using a Wilcoxon signed-rank paired test.

CEUS results indicating a strong reduction in vascularization in terms of vascular distribution (unperfused area and PE, Fig. 6) and functionality (MTT, WOR, WIR: Table 1, Fig. 6).

Summary of changes in all the parameters considered

The ultrasound frequency range varied somewhat between modalities because of equipment-related constraints and choices made to obtain the highest signal quality. In particular, for QUS, higher frequencies (>10 MHz) were needed because spectral analysis requires a sufficient number of samples to produce estimates with low bias and variance. Specifically, the variance of the estimates is directly related to the number of resolution cells used in calculation of the spectral parameters. Because of the small size of the mouse tumors, a higher-frequency probe was used to reduce the resolution cell size and enable a larger number of data blocks to be processed for each tumor.

Table 1 summarizes the percentage variation of each measured parameter from the start to the end of therapy. During cytotoxic therapy, only the SWE was significantly modified. The increase in tumor stiffness for the cytotoxic group was three to four times lower than that for other groups. Tumors treated with the anti-angiogenic drug underwent the highest variations in parameters measured by SWE and CEUS between baseline and the end of the study. However, a similar level of SWE and CEUS modification was observed in the placebo group (Fig. 3). The action of sunitinib, which targets essentially the TME of tumor cells, created a very heterogeneous pattern revealed by *in vivo* imaging in terms of increased SD for the stiffness and vascular distribution parameters. This heterogeneity in the tumor composition was confirmed by histology outcomes.

The evaluation of correlations between parameters measured longitudinally with different ultrasound modes can provide additional useful information (Fig. 8). Considering the two different classes of parameters, those related to the microvascularization (vascular function) and those related to stroma structure (micro/macroscopic level), intra-correlations occur between parameters from the same class and inter-correlations occur between parameters from two different classes. Similar intra-correlations can be observed for each therapy group (except for EAC and ESD parameters) Inter-correlations, however, are very different from one group to another. The anti-angiogenic, placebo and cytotoxic groups had respectively 22, 8 and 2 inter-correlations ($r > 0.4$).

Thus, the evolution of mean parameter values provides information that can differentiate between groups, as described in Table 1, which indicates that the tumors undergoing the most significant changes were those treated with anti-angiogenic drug. Beyond that, however, it seems that inter-correlations offer another point of view to characterize the level of modifications within tumors, and as illustrated in Figure 8, specific patterns of correlation can be distinguished between the three therapy groups.

CONCLUSIONS

In summary, individual parameters are influenced by a relatively complex combination of underlying modifications in the tumor. Observation of parameter modifications in specific tumor models allows the identification of changes in response to a relatively fixed set of changes in the tumor composition. Within the LLC model, modifications of parameters observed with CEUS reflected changes in the flow and distribution of the functional microvessels that are consistent with what is anticipated during anti-angiogenic therapy. Both tumor stiffness and QUS microstructure parameters appeared to be modified systematically as the level of fibrosis in the tumors increased. As tumor composition became more heterogeneous and complex, greater correlation was observed between functional and structural image-based assessments. Identifying such parameter–TME relationships in specific types of tumors should ultimately enable a

more physiologic, multiparametric assessment when SWE, QUS and CEUS are used to monitor tumor response to therapy.

REFERENCES

Athanasiou A, Latorre-Ossa H, Criton A, Tardivon A, Gennisson J, Tanter M. Feasibility of imaging and treatment monitoring of breast lesions with three-dimensional shear wave elastography. Ultraschall Med 2015;38:51–59.

Barrois G, Coron A, Payen T, Dizeux A, Bridal L. A multiplicative model for improving microvascular flow estimation in dynamic theory and experimental validation. IEEE Trans Ultrason Ferroelectr Freq Control 2013;60:2284–2294.

Battle MR, Goggi JL, Allen L, Barnett J, Morrison MS. Monitoring tumor response to antiangiogenic sunitinib therapy with ^{18}F-fluciclatide, an ^{18}F-labeled αVbeta3-integrin and α beta5-integrin imaging agent. J Nucl Med 2011;52:424–430.

Bozkurt D, Sarsik B, Hur E, Ertilav M, Burcak K, Ozge T, Selahattin B, Fehmi A, Soner D. A novel angiogenesis inhibitor, sunitinib malate, in encapsulating peritoneal sclerosis. J Nephrol 2011;24:359–365.

Broutin S, Ameur N, Lacroix L, Robert T, Petit B, Oumata N, Talbot M, Caillou B, Schlumberger M, Dupuy C, Bidart JM. Identification of soluble candidate biomarkers of therapeutic response to sunitinib in medullary thyroid carcinoma in preclinical models. Clin Cancer Res 2011;17:2044–2054.

Chamming's F, Latorre-Ossa H, Le Frère-Belda MA, Fitoussi V, Quibel T, Assayag F, Marangoni E, Autret G, Balvay D, Pidial L, Gennisson JL, Tanter M, Cuenod CA, Clément O, Fournier LS. Shear wave elastography of tumour growth in a human breast cancer model with pathological correlation. Eur Radiol 2013;23:2079–2086.

Chauvet D, Imbault M, Capelle L, Demene C, Mossad M, Karachi C, Boch A, Gennisson J, Tanter M. In vivo measurement of brain tumor elasticity using intraoperative shear wave elastography. Ultraschall Med 2015;37:584–590.

Chen X, Phillips D, Schwarz K, Mottley J, Parker K. The measurement of backscatter coefficient from a broadband pulse-echo system: A new formulation. IEEE Trans Ultrason Ferroelectr Freq Control 1997;44:515–525.

Dietrich C, Averkiou M, Correas J, Lassau N, Leen E, Piscaglia F. An EFSUMB introduction into dynamic contrast-enhanced ultrasound (DCE-US) for quantification of tumour perfusion. Ultraschall Med 2012;33:344–351.

Dizeux A, Payen T, Barrois G, Le Guillou Buffello D, Bridal SL. Reproducibility of contrast-enhanced ultrasound in mice with controlled injection. Mol Imaging Biol Mol Imaging Biol 2016;18:651–658.

El Kaffas A, Sadeghi-Naini A, Falou O, Tran WT, Zhou S, Hashim A, Fernandes J, Giles A, Czarnota GJ. Assessment of tumor response to radiation and vascular targeting therapy in mice using quantitative ultrasound spectroscopy. Med Phys 2015;42:4965–4973.

Errico C, Pierre J, Pezet S, Desailly Y, Lenkei Z, Couture O, Tanter M. Ultrafast ultrasound localization microscopy for deep super-resolution vascular imaging. Nature 2015;527:499–502.

Faivre S, Demetri G, Sargent W, Raymond E. Molecular basis for sunitinib efficacy and future clinical development. Nat Rev Drug Discov 2007;6:734–745.

Guibal A, Taillade L, Mulé S, Comperat E, Badachi Y, Golmard JL, Rixe O, Bridal SL, Lucidarme O. Noninvasive contrast-enhanced US quantitative assessment of tumor microcirculation in a murine model: Effect of discontinuing anti-VEGF therapy. Radiology 2010;254:420–429.

Hillman GG, Singh-Gupta V, Zhang H, Al-Bashirt AK, Katkuri Y, Li M, Yunker CK, Patel AD, Abrams J, Haacke EM. Dynamic contrast-enhanced magnetic resonance imaging of vascular changes induced by sunitinib in papillary renal cell carcinoma xenograft tumors. Neoplasia 2009;11:910–920.

Hompland T, Ellingsen C, Øvrebø KM, Mri C. Interstitial fluid pressure and associated lymph node metastasis revealed in tumors by dynamic contrast-enhanced MRI. Cancer Res 2012;72:4899–4908.

Huang D, Ding Y, Li Y, Luo W-M, Zhang Z-F, Snider J, Vandenbeldt K, Qian CN, Teh BT. Sunitinib acts primarily on tumor endothelium rather than tumor cells to inhibit the growth of renal cell carcinoma. Cancer Res 2010;70:1053–1062.

Hudson JM, Williams R, Tremblay-Darveau C, Sheeran PS, Milot L, Bjarnason GA, Burns PN. Dynamic contrast enhanced ultrasound for therapy monitoring. Eur J Radiol 2015;84:1650–1657.

Hyvelin JM, Tardy I, Arbogast C, Costa M, Emmel P, Helbert A, Theraulaz M, Nunn AD. Use of ultrasound contrast agent microbubbles in preclinical research: Recommendations for small animal imaging. Invest Radiol 2013;48:571–583.

Jain RK. Normalizing tumor microenvironment to treat cancer: Bench to bedside to biomarkers. J Clin Oncol 2013;31:2205–2218.

Jugé L, Doan B-T, Seguin J, Albuquerque M, Larrat B, Mignet N, Chabot GG, Scherman D, Paradis V, Vilgrain V, Van Beers BE, Sinkus R. Colon tumor growth and antivascular treatment in mice: Complementary assessment with MR elastography and diffusion-weighted MR imaging. Radiology 2012;264:436–444.

Kemmerer JP, Ghoshal G, Karunakaran C, Oelze ML. Assessment of high-intensity focused ultrasound treatment of rodent mammary tumors using ultrasound backscatter coefficients. J Acoust Soc Am 2013;134:1559–1568.

Kolios M, Czarnota G. Potential use of ultrasound for the detection of cell changes in cancer treatment. Future Oncol 2009;5:1527–1532.

Kolios M, Czarnota G, Lee M, Hunt J, Sherar M. Ultrasonic spectral parameter characterization of apoptosis. Ultrasound Med Biol 2002;28:589–597.

Leen E, Averkiou M, Arditi M, Burns P, Bokor D, Gauthier T, Kono Y, Lucidarme O. Dynamic contrast enhanced ultrasound assessment of the vascular effects of novel therapeutics in early stage trials. Eur Radiol 2012;22:1442–1450.

Lowe S, Lin A. Apoptosis in cancer. Carcinogenesis 2000;21:485–495.

Matsumoto S, Batra S, Saito K, Yasui H, Choudhuri R, Gadisetti C, Subramanian S, Devasahayam N, Munasinghe JP, Mitchell JB, Krishna MC. Antiangiogenic agent sunitinib transiently increases tumor oxygenation and suppresses cycling hypoxia. Cancer Res 2011;71:6350–6359.

Matsumoto S, Saito K, Takakusagi Y, Matsuo M, Munasinghe JP, Morris HD, Lizak MJ, Merkle H, Yasukawa K, Devasahayam N, Suburamanian S, Mitchell JB, Krishna MC. In vivo imaging of tumor physiological, metabolic, and redox changes in response to the anti-angiogenic agent sunitinib: Longitudinal assessment to identify transient vascular renormalization. Antioxid Redox Signal 2014;10:1145–1155.

Mendel DB, Laird AD, Xin X, Louie SG, Christensen JG, Li G, Schreck RE, Abrams TJ, Ngai TJ, Lee LB, Murray LJ, Carver J, Chan E, Moss KG, Joshua O, Sukbuntherng J, Blake RA, Sun L, Tang C, Miller T, Shirazian S, Mcmahon G, Cherrington JM. In vivo antitumor activity of SU11248, a novel tyrosine kinase inhibitor targeting vascular endothelial growth factor and platelet-derived growth factor receptors: Determination of a pharmacokinetic/pharmacodynamic relationship. Clin Cancer Res 2003;9:327–337.

Nakasone E, Askautrud H, Kees T, Park J, Plaks V, Ewalds A, Fein M, Rasch M, Tan Y, Qiu J, Park J, Sinha P, Bissell M, Frenqen E, Werb Z, Egeblad M. Imaging tumor–stroma interactions during chemotherapy reveals contributions of the microenvironment to resistance. Cancer Cell 2012;21:488–503.

Needles A, Heinmiller A, Sun J, Theodoropoulos C, Bates D, Hirson D, Yin M, Foster FS. Development and initial application of a fully integrated photoacoustic micro-ultrasound system. IEEE Trans Ultrason Ferroelectr Freq Control 2013;60:888–897.

Payen T, Coron A, Lamuraglia M, Le Guillou-Buffello D, Gaud E, Arditi M, Lucidarme O, Bridal SL. Echo-power estimation from log-compressed video data in dynamic contrast-enhanced ultrasound imaging. Ultrasound Med Biol 2013;39:1826–1837.

Payen T, Dizeux A, Baldini C, Le Guillou-Buffello D, Lamuraglia M, Comperat E, Lucidarme O, Bridal SL. VEGFR2-targeted contrast-enhanced ultrasound to distinguish between two anti-angiogenic treatments. Ultrasound Med Biol 2015;41:2202–2211.

Rao SR, Shelton SE, Dayton PA. The "fingerprint" of cancer extends beyond solid tumor bondaries: Assessment with a novel ultrasound imaging approach. IEEE Trans Biomed Eng 2016; 63:1082–1086.

Sannachi L, Taddayyon H, Sadeghi-Naini A, Tran W, Gandhi S, Wright F, Oelze ML, Czarnota G. Non-invasive evaluation of breast cancer response to chemotherapy using quantitative ultrasonic backscatter parameters. Med Image Anal 2015;20:224–236.

Tanter M, Fink M. Ultrafast imaging in biomedical ultrasound. IEEE Trans Ultrason Ferroelectr Freq Control 2014;61:102–119.

Vlad R, Alajez N, Giles A, Kolios M, Czarnota G. Quantitative ultrasound characterization of cancer radiotherapy effects in vitro. Int J Radiat Oncol Biol Phys 2008;72:1236–1243.

Vlad R, Brand S, Giles A, Kolios M, Czarnota G. Quantitative ultrasound characterization of responses to radiotherapy in cancer mouse models. Clin Cancer Res 2009;15:2067–2075.

Vlad R, Kolios M, Moseley J, Czarnota G, Brock K. Evaluating the extent of cell death in 3-D high frequency ultrasound by registration with whole-mount tumor histopathology. Med Phys 2010;37: 4288–4297.

Vlad R, Kolios M, Czarnota G. Ultrasound imaging of apoptosis: Spectroscopic detection of DNA-damage effects at high and low frequencies. Methods Mol Biol 2011;682:165–187.

Wang X, Zhang J, Xu T. Cyclophosphamide as a potent inhibitor of tumor thioredoxin reductase in vivo. Toxicol Appl Pharmacol 2007; 218:88–95.

Williams R, Hudson JM, Lloyd BA, Sureshkumar AR, Lueck G, Milot L, Atri M, Bjarnason GA, Burns PN. Dynamic microbubble contrast-enhanced US to measure tumor response to targeted therapy: a proposed clinical protocol with results from renal cell carcinoma patients receiving antiangiogenic therapy. Radiology 2011; 260:581–590.